

AC Fingerprints of 2D Electron Hydrodynamics: Superdiffusion and Drude Weight Suppression

Davis Thuillier¹ and Thomas Scaffidi^{1, *}

¹*Department of Physics, University of California, Irvine, Irvine, CA 92697, USA*

(Dated: 16 March 2026)

Clean two-dimensional Fermi liquids are now known to exhibit an intermediate *tomographic* regime, between ballistic and Navier–Stokes transport, caused by the anomalously slow relaxation of parity-odd multipolar deformations of the Fermi surface. Here we show that this anomaly extends to the dynamical realm. Starting from a microscopic numerical evaluation of the linearized electron–electron collision operator, we find that the finite-frequency nonlocal conductivity is controlled at low frequency by a single hydrodynamic pole, $\sigma(q, \omega) = \mathcal{D}(q)/(i\omega + \eta_* q^z)$, with dynamical exponent $z = 4/3$ and superdiffusive viscosity η_* . Remarkably, the pole residue itself is scale dependent and obeys $\mathcal{D}(q) \sim q^{-\alpha}$ with $\alpha = 1/3$, so the dynamical properties are described by two separate exponents rather than one. We interpret the residue suppression using a Krylov-chain description of current relaxation: as q increases, the longest-lived quasinormal mode ceases to be a nearly pure current excitation and spreads over higher odd angular harmonics. Finally, we show that AC transport in narrow channels provides a direct route to measuring the exponents z and α separately.

Hydrodynamics is a powerful framework for describing interacting many-body systems, and recent progress in ultra-clean metals has shown its relevance to electronic transport. In this regime, momentum-conserving electron collisions dominate over momentum-relaxing ones, allowing viscosity to control transport. This possibility has driven substantial theoretical [1–30] and experimental [31–43] activity. It is by now well understood that viscous effects can be observed in certain metals through size-dependent transport, as captured by the non-local conductivity $\sigma(q)$.

A fundamental question raised by these developments is whether microscopic quantum kinetics can produce emergent hydrodynamic theories that differ qualitatively from the Navier–Stokes paradigm. Low-dimensional systems provide natural settings for such behavior. In quantum spin chains, for example, spin and energy transport can become superdiffusive [44–49], with a dynamical exponent z lying between the ballistic value $z = 1$ and the diffusive value $z = 2$.

Two-dimensional Fermi liquids provide another striking example. Because of the special form of Pauli blocking in two dimensions, parity-odd angular harmonics of the quasiparticle distribution near the Fermi surface relax parametrically more slowly than parity-even ones [17, 18, 21–23, 25–29]. As a result, clean 2D Fermi liquids exhibit two distinct regimes of hydrodynamic behavior: at large length scales, 2D Fermi liquids behave like a conventional viscous fluid described by the Navier–Stokes equation with non-local transverse conductivity $\sigma(q) \sim q^{-2}$; at intermediate scales, however, they enter a tomographic regime with fractional scaling $\sigma(q) \sim q^{-5/3}$ due to the long-lived odd modes [50].

Here we are interested in how these hydrodynamic effects extend to the *dynamical* realm, which is captured by the finite-frequency non-local conductivity $\sigma(q, \omega)$.

In the Navier–Stokes regime, going to finite frequency is fairly trivial: one finds a diffusive pole $\sigma(q, \omega) = 1/(i\omega + \eta q^2)$, and the dynamical exponent $z = 2$ could thus have been inferred directly from the static conductivity decaying as $\sigma(q, 0) \sim q^{-2}$. By contrast, we will show that the dynamical conductivity in the tomographic regime is considerably richer than its static limit suggests. We find that the low-frequency transverse conductivity is governed by a pole of the form,

$$\sigma(q, \omega) = \frac{\mathcal{D}(q)}{i\omega + \eta_* q^z}, \quad (1)$$

with dynamical exponent $z = 4/3$ and superdiffusive viscosity η_* . Crucially, the residue $\mathcal{D}(q)$, which can be interpreted as a finite- q Drude weight, is itself scale dependent:

$$\mathcal{D}(q) \sim q^{-\alpha}, \quad \alpha = \frac{1}{3}. \quad (2)$$

The static scaling $\sigma(q, 0) \sim q^{-5/3}$ therefore arises from the combination of a superdiffusive decay rate and an anomalously suppressed residue. The tomographic regime is thus characterized by two exponents, z and α , rather than one.

We first compute the spectrum of the linearized electron–electron collision operator and verify the strong even–odd hierarchy of relaxation rates characteristic of 2D Fermi liquids. We then reformulate the finite- q current dynamics as a diffusion-dissipation model on a Krylov chain, which yields the prediction of Eq. (1). Next, we confirm these predictions with numerical calculations and we show how logarithmic corrections to the even decay rates govern the slow approach of the exponents z and α to their asymptotic values. Finally, we show how to use AC transport in narrow channels to probe these effects experimentally.

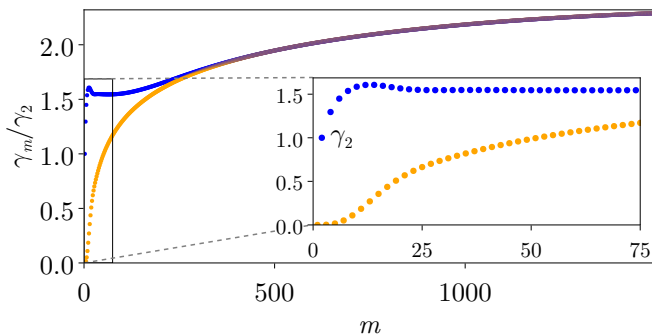


FIG. 1. Spectrum of the linearized interparticle collision operator in the cylindrical-harmonic basis, shown as the decay rates $\gamma_{m,\text{even}}$ in blue and $\gamma_{m,\text{odd}}$ in orange at $T/T_F = 0.005$. One can observe the different behavior of the even and odd rates for $m \leq m_{\text{max}} \approx 12$ as discussed around Eqs. 4 and 5.

While our focus is on the universal pole structure of $\sigma(q, \omega)$, recent work has explored other dynamical consequences of the even-odd hierarchy, including cyclotron resonances [26], finite-frequency modifications of the Gurzhi dip [51], and collective modes in idealized tomographic spectra with distinct even and odd relaxation rates [21, 52].

Boltzmann equation and collision spectrum.— We consider the Boltzmann transport equation for a clean two-dimensional Fermi liquid at $T \ll T_F$. A weak deformation $\delta f(\mathbf{r}, \mathbf{k}, t) = (-\partial n_F / \partial \varepsilon_{\mathbf{k}}) \chi(\mathbf{r}, \mathbf{k}, t)$ away from the Fermi-Dirac distribution evolves according to the Boltzmann Transport Equation (BTE):

$$\partial_t \chi + \mathbf{v} \cdot \nabla_{\mathbf{r}} \chi + L[\chi] = e \mathbf{v} \cdot \mathbf{E}, \quad (3)$$

where L is the linearized electron-electron collision operator, \mathbf{E} is the applied electric field, and $\mathbf{v} = v_F(\cos(\theta), \sin(\theta))$ is the quasiparticle velocity at the Fermi surface (FS), with θ the angle around the FS [53].

In order to solve this equation, the first step is to calculate the collision operator L . We evaluate it numerically for a local repulsive interaction using the method introduced in [30]; see the Supplemental Material (SM) [54] for details. Using rotational invariance, and in the limit $T \ll T_F$, the collision operator is fully characterized by decay rates γ_m for the angular harmonics of the angular distribution $\chi(\theta)$ of quasiparticles at the Fermi surface $L[e^{im\theta}] = \gamma_m e^{im\theta}$, and with $\gamma_0 = \gamma_1 = 0$ due to conservation of particle number and momentum.

The resulting spectrum, shown in Figure 1, exhibits the expected even-odd hierarchy, with even modes decaying much faster than odd ones due to the specifics of Pauli blocking in 2D, as explained in Refs. [17, 18, 29]. Rates for even harmonics are approximately constant in m : they increase only slowly with m up to $m_{\text{max}} \sim (T/T_F)^{-1/2}$ after which they saturate, following [55]

$$\gamma_{m,\text{even}} = \gamma_2 F[m], \quad (4)$$

with $\gamma_2 \propto T^2/T_F$ and where $F[m] = \sum_{j=1}^{m/2} \frac{1}{2j-1}$ is a slowly increasing function of m such that $F[2] = 1$ and $F[m \rightarrow \infty] \sim \frac{1}{2} \log m$.

Decay rates of odd harmonics grow as m^4 up to m_{max} , after which they saturate. For $m \geq 3$, Ref. [55] obtained

$$\gamma_{m,\text{odd}} = \gamma_3 \left(\frac{m}{3}\right)^4. \quad (5)$$

with $\gamma_3 \propto T^4/T_F^3$. When performing calculations, we will use our numerically obtained spectra for $T/T_F \geq 0.005$, and the analytic expressions (4) and (5) when studying lower T/T_F .

Diffusion-dissipation dynamics on the Krylov chain.— To understand the pole structure of the transverse $\sigma(q, \omega)$, it is useful to start with the real-time relaxation of a current flowing along x and modulated along y , $\mathbf{j}(y, t) = e^{iqy} j_q(t) \hat{\mathbf{x}}$, with initial condition $j_q(0) = 1$.

The initial current corresponds in the BTE to the initial condition $\chi(y, \theta, t = 0) = e^{iqy} \cos \theta$. Omitting the e^{iqy} factor henceforth, we expand $\chi(\theta, t) = \sum_{m \geq 1} \varphi_m(t) f_m(\theta)$, with

$$f_m(\theta) = \begin{cases} \cos(m\theta), & m \text{ odd}, \\ -i \sin(m\theta), & m \text{ even}, \end{cases} \quad (6)$$

where the coefficients $\varphi_m(t)$ may be viewed as a wavefunction on a semi-infinite one-dimensional ‘‘Krylov’’ chain [57] whose site index m labels angular harmonics of the FS deformation.

The Boltzmann equation then takes the form

$$\partial_t \varphi_m = \frac{q}{2} (\varphi_{m-1} - \varphi_{m+1}) - \gamma_m \varphi_m, \quad m \geq 1, \quad (7)$$

with $\varphi_0 \equiv 0$. The q -dependent term generates hopping along the chain, while the collision operator produces site-dependent decay. We focus on m below m_{max} , in which case $\gamma_{2n} \gg \gamma_{2n-1}$, and the even sites may thus be eliminated adiabatically: $\varphi_{2n} \simeq \frac{q}{2\gamma_{2n}} (\varphi_{2n-1} - \varphi_{2n+1})$. Approximating for now the even rates as constant ($\gamma_{2n} \approx \gamma_2$), the dynamics of the odd modes reads:

$$\begin{aligned} \partial_t \varphi_1 &= \frac{q^2}{4\gamma_2} (\varphi_3 - \varphi_1) \\ \partial_t \varphi_{m \geq 3} &= \frac{q^2}{4\gamma_2} (\varphi_{m-2} - 2\varphi_m + \varphi_{m+2}) - \gamma_m \varphi_m, \end{aligned} \quad (8)$$

with $\varphi_m(0) = \delta_{m,1}$ and $j_q(t) = \varphi_1(t)$.

For $q \ll q_{\text{min}}$ (with $q_{\text{min}} \equiv \sqrt{\gamma_2 \gamma_3}$), it is easy to show that $\varphi_{m \geq 3}$ is negligible, in which case the current reads

$$j_q(t) \sim e^{-\eta q^2 t} \quad (\text{Navier-Stokes}), \quad (9)$$

with $\eta = 1/(4\gamma_2)$ the viscosity. This is the familiar Navier-Stokes regime.

By contrast, in the tomographic regime for $q \gg q_{\text{min}}$, one needs to solve the full set of equations in (8), which is

a discrete diffusion-dissipation model with diffusion constant $d_q \equiv q^2/\gamma_2$ and dissipation rates set by $\gamma_{m,\text{odd}}$. Since the wavefunction now spreads over many odd sites, we take the continuum limit $m \rightarrow m \in \mathbb{R}$. One then obtains $-\partial_t \varphi(m, t) = H\varphi(m, t)$ with

$$H = -d_q \partial_m^2 + V(m), \quad (10)$$

a 1D Schrödinger operator: the diffusion term $-d_q \partial_m^2$ plays the role of a kinetic energy, while dissipation acts as a confining potential, $V(m) = \gamma_{m,\text{odd}} \propto \gamma_3 |m|^p$.

After diagonalizing the Hamiltonian,

$$H\phi_\mu(m) = \epsilon_\mu \phi_\mu(m), \quad (11)$$

with eigenvalues ordered as $0 < \epsilon_0 < \epsilon_1 < \dots$, one has

$$j_q(t) = \sum_\mu |\phi_\mu(m=0)|^2 e^{-\epsilon_\mu t} \quad (12)$$

since $j_q(t)$ in the continuum limit becomes the return amplitude $\varphi(m=0, t)$ of a wavepacket initially localized at $m=0$ [58].

For $p=4$, $V(m) \propto m^4$, and H describes a quantum-mechanical quartic oscillator with low-energy eigenstates $\phi_\mu(m)$ forming a discrete set of localized states with a characteristic extent $\langle m \rangle$ set by balancing kinetic and potential energy:

$$d_q/\langle m \rangle^2 \sim \gamma_3 \langle m \rangle^p \implies \langle m \rangle \sim (d_q/\gamma_3)^{1/(p+2)}. \quad (13)$$

Similarly, the corresponding eigenvalues scale as $\epsilon_\mu \sim \gamma_3 (d_q/\gamma_3)^{p/(p+2)}$.

At early times, the initial wave packet is localized near the origin, the confining potential is negligible, and the wave packet simply diffuses, so its extent grows as $m(t) \sim \sqrt{d_q t}$. This gives a power-law decay of the current

$$j_q(t) \sim \frac{1}{\sqrt{d_q t}}, \quad t \ll t(q) \quad (14)$$

which continues until a time $t(q) \sim \langle m \rangle^2/d_q$, when the spreading of the wavepacket saturates at $m(t) \sim \langle m \rangle$.

At later times, the finite gap to the first excited state in the spectrum of H [59] justifies keeping only the ‘‘ground state’’ $\phi_0(m)$ in (12):

$$j_q(t) \simeq \mathcal{D}(q) e^{-\gamma(q)t}, \quad t \gg t(q) \quad (15)$$

with $\gamma(q) \equiv \epsilon_0(q)$ and $\mathcal{D}(q) \equiv |\phi_0(m=0)|^2$. Using the scaling found above for the spectrum of H , we obtain

$$\gamma(q) \sim \gamma_3 \left(\frac{q}{q_{\min}} \right)^z, \quad z = \frac{2p}{p+2} = \frac{4}{3}. \quad (16)$$

Likewise, since the ground state is spread over $\sim \langle m \rangle$ sites, one finds $\mathcal{D}(q) \sim \langle m \rangle^{-1}$ and thus

$$\mathcal{D}(q) \sim \left(\frac{q}{q_{\min}} \right)^{-\alpha}, \quad \alpha = \frac{2}{p+2} = \frac{1}{3}. \quad (17)$$

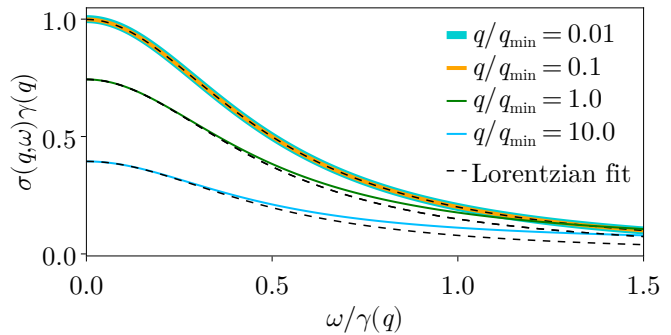


FIG. 2. Finite-frequency nonlocal conductivity $\sigma(q, \omega)$ at $T/T_F = 0.005$. The low-frequency line shape is well fit by a Lorentzian, $\sigma(q, \omega) = \mathcal{D}(q)/(i\omega + \gamma(q))$, from which we extract the decay rate $\gamma(q)$. Rescaling the vertical axis by $\gamma(q)$ and the horizontal axis by $1/\gamma(q)$ would collapse the curves if the residue were constant. This collapse is observed for the two curves with $q \ll q_{\min}$, while the two curves with $q \gtrsim q_{\min}$ are progressively suppressed, indicating a decreasing residue.

Overall, the real-time dynamics in the tomographic regime differs qualitatively from Navier–Stokes because the longest-lived mode is spread over a parametrically large number of odd harmonics, rather than being an almost purely dipolar excitation. Consequently, $j_q(t)$ first decays as $1/\sqrt{t}$ while the wavepacket diffuses across the full extent of this mode, and only then crosses over to exponential decay, $j_q(t) \sim \mathcal{D}(q)e^{-\gamma(q)t}$, with a parametrically small prefactor $\mathcal{D}(q) \ll 1$. In frequency space, this becomes the suppressed pole residue of the conductivity, as we now show.

AC conductivity.— Up to an overall prefactor[60], the nonlocal transverse conductivity is

$$\sigma(q, \omega) = \int_0^\infty dt j_q(t) e^{-i\omega t}. \quad (18)$$

In the Navier–Stokes regime, plugging (9) in this integral gives the familiar diffusive pole,

$$\sigma(q, \omega) = \frac{1}{i\omega + \eta q^2} \quad (\text{Navier–Stokes}). \quad (19)$$

In the tomographic regime, inserting (15) instead yields

$$\sigma(q, \omega) \approx \frac{\mathcal{D}(q)}{i\omega + \gamma(q)} = \frac{\tilde{q}^{-\alpha}}{i\omega + \eta_* q^z}, \quad (20)$$

with $\tilde{q} \equiv q/q_{\min}$ and where $\eta_* \equiv \gamma_3/q_{\min}^z$ is the superdiffusive version of the viscosity. We thus find that the hydrodynamic pole is described by two exponents, the dynamical exponent z describing the superdiffusive scaling of the decay rate $\gamma(q)$, and the exponent α controlling the suppression of the pole residue (or finite- q Drude weight) $\mathcal{D}(q)$.

Another formulation of (20) is the fractional Stokes equation

$$\partial_t \mathbf{j} = -\eta_* |\nabla|^z \mathbf{j} + q_{\min}^\alpha |\nabla|^{-\alpha} \mathbf{E}, \quad (21)$$

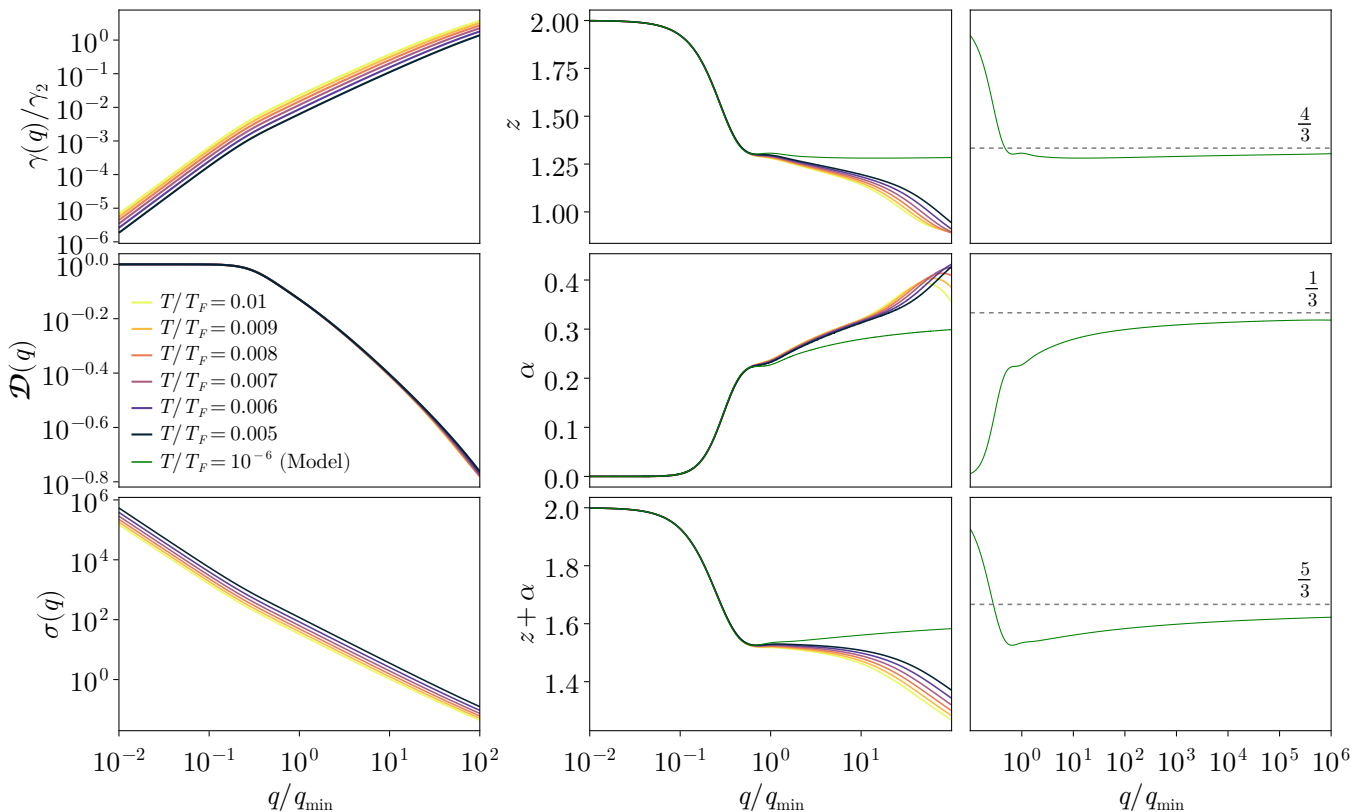


FIG. 3. (Left column) Extracted $\gamma(q)$, $\mathcal{D}(q)$, and $\sigma(q, \omega = 0)$ for a range of temperatures. (Middle column) Local exponents calculated by logarithmic derivatives, i.e., $z(q) \equiv d \ln \gamma / d \ln q$ and $\alpha \equiv d \ln \mathcal{D} / d \ln q$, plotted versus q/q_{\min} . (Right column) Local exponents shown over a larger range of q/q_{\min} , for $T/T_F = 10^{-6}$, demonstrating the slow approach to their asymptotic values.

where the gradient is taken transverse to \mathbf{E} . This equation applies over the tomographic range $q_{\min} \ll q \ll \gamma_2$.

Numerical confirmation.— We now compare these predictions with $\sigma(q, \omega)$ computed numerically from the full spectrum of decay rates using the continued-fraction representation of Ref. [50]. Figure 2 shows a representative set of line shapes. At low frequency, the conductivity is very well fit by a Lorentzian, which justifies the single-pole form and allows us to extract $\gamma(q)$ and $\mathcal{D}(q)$ through a fit to $\sigma(q, \omega) = \frac{\mathcal{D}(q)}{i\omega + \gamma(q)}$.

The extracted quantities are shown in Fig. 3. As expected, one recovers the Navier–Stokes regime for $q \ll q_{\min}$, with $\gamma(q) \sim q^2$ and $\mathcal{D}(q) = 1$. For $q \gtrsim q_{\min}$, we observe a crossover to the tomographic regime: the decay rate crosses over to $\gamma(q) \sim q^z$ with z approaching $4/3$, and the residue starts to decay as $\mathcal{D}(q) \sim q^{-\alpha}$ with α approaching $1/3$.

We observe that the approach with q/q_{\min} of the “local exponents” $z(q)$ and $\alpha(q)$ towards their asymptotic value is slow, see Fig. 3 right column. We attribute this to the weak increase with m of the even rates (see Eq. 4), which we have neglected so far. Since $F[m]$ grows as $\frac{1}{2} \log m$, the effective diffusion constant along the Krylov chain becomes m dependent, $d_q \sim q^2 / (\gamma_2 F[m])$. Equation (13) is

then replaced by $F[m]m^{p+2} \sim (q/q_{\min})^2$. This motivates an effective exponent

$$p_{\text{eff}}[m] \equiv \frac{d \log(F[m]m^p)}{d \log m} \sim p + \frac{1}{\log m/2 + \gamma}, \quad (22)$$

with γ the Euler–Mascheroni constant (see SM). Equivalently, the observed exponents may be viewed as scale dependent, with $\alpha(q) = 2/[p_{\text{eff}}(q) + 2]$ and $z(q) = p\alpha(q)$, where $p_{\text{eff}}(q) \equiv p_{\text{eff}}[m(q)]$ and $m(q)$ is determined by Eq. 13. As q/q_{\min} increases, $m(q)$ increases as well, reducing the logarithmic correction and driving $p_{\text{eff}} \rightarrow 4$, $\alpha \rightarrow 1/3$, and $z \rightarrow 4/3$. In practice, however, the accessible range of q/q_{\min} is upper bounded by the crossover to the ballistic regime, so experimentally measured exponents will typically remain below their asymptotic values, an important point when comparing with tomographic-regime experiments such as Ref. [43].

AC conductance of a narrow channel.— A natural way to probe $\sigma(q, \omega)$ experimentally is through AC transport in a channel of width W . In the tomographic regime, where $W \ll q_{\min}^{-1}$ so that the relevant transverse wave numbers satisfy $q \sim 1/W \gg q_{\min}$, the low-frequency

channel conductance inherits the same pole structure:

$$\frac{G(W, \omega)}{W} \equiv \frac{\mathcal{D}(W)}{i\omega + \gamma(W)} \sim \frac{q_{\min}^\alpha W^\alpha}{i\omega + \eta_* W^{-z}}. \quad (23)$$

This “finite-width Drude peak” provides a direct way to measure z and α separately by considering channels of varying width. The width of the peak scales as W^{-z} , while its height scales as $G(\omega = 0)/W \sim W^{z+\alpha}$. Equivalently, the total spectral weight under the peak scales as W^α , giving a direct probe of the residue suppression.

We verify this behavior numerically in Fig. 4 (see SM for details of the channel calculations), using representative parameters for clean 2D metals like graphene. We also include momentum relaxation through $\gamma_{m \geq 1} \rightarrow \gamma_{m \geq 1} + \gamma_{\text{MR}}$. This introduces an upper bound in channel width above which the bulk Drude peak is recovered with $\gamma(W) \approx \gamma_{\text{MR}}$ and $D(W) \approx 1$. For narrower channels, however, the suppression of the hydrodynamic spectral weight is observable, see Fig. 4 bottom panel.

One may also work at fixed width and vary temperature within the tomographic range. Since $q_{\min} \propto T^3$ and $\eta_* \propto T^{4-3z}$, the peak height is predicted to scale as $G(\omega = 0)/W \sim T^{3(z+\alpha)-4}$ while the peak width scales as $\gamma \sim T^{4-3z}$. At the asymptotic values $z = 4/3$ and $\alpha = 1/3$, the peak height is linear in T (as predicted in Ref. [29]) while the peak width is T independent, although the logarithmic drift of exponents discussed above implies noticeable deviations at realistic temperatures. The total Drude spectral weight increases with temperature as $T^{3\alpha}$, which is T -linear for $\alpha \rightarrow 1/3$. Overall, the T -linear increase of the DC conductance in the tomographic regime [29] thus results from a T -linear Drude weight rather than from a temperature-dependent decay rate.

High frequencies and boundary layers.— So far we have focused on low frequencies $\omega \lesssim \gamma(W)$. At higher frequencies a different regime appears: the in-phase current becomes confined to boundary layers near the channel walls [11]. For a dynamical exponent z , the boundary-layer width is expected to scale as $\delta \sim (\frac{\eta}{\omega})^{1/z}$. In the End Matter, we confirm this prediction numerically, showing a crossover of the form:

$$\delta \sim \begin{cases} (\eta/\omega)^{1/2}, & \text{Navier–Stokes } (\omega \ll \gamma_3), \\ (\eta_*/\omega)^{3/4} & \text{Tomographic } (\omega \gg \gamma_3). \end{cases} \quad (24)$$

We also give the corresponding frequency and temperature dependence of the channel conductance at high frequencies. For quasi-2D bulk metals, we expect that similar tomographic effects in boundary-layer physics should be observable via the skin effect [61].

Conclusion.— We have shown that the finite-frequency nonlocal conductivity of clean 2D Fermi liquids in the tomographic regime is controlled by a single hydrodynamic pole, $\sigma(q, \omega) \sim \frac{\mathcal{D}(q)}{i\omega + \eta_* q^z}$, with $z = 4/3$ and a

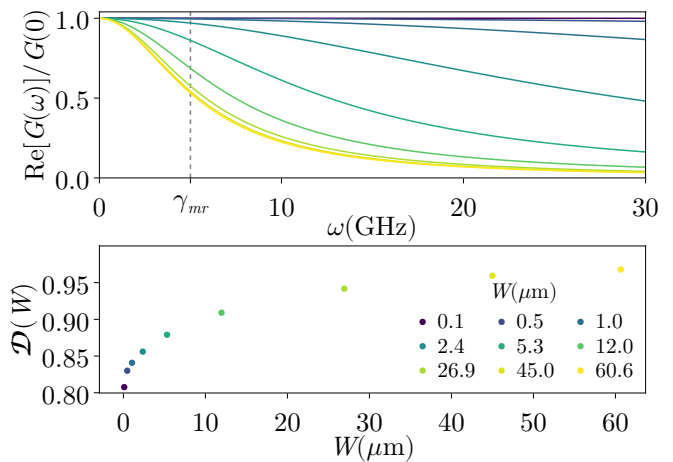


FIG. 4. Top: Channel conductance for several widths W , computed at $T/T_F = 0.005$ with $v_F = 10^6$ m/s and with an overall scale of the collision operator chosen so that $\gamma_3 = 5$ GHz. Momentum relaxation with $\gamma_{\text{MR}} = 5$ GHz is also included. Bottom: Pole residue extracted by fitting the low-frequency channel conductance to $G(\omega)/W = \mathcal{D}/(i\omega + \gamma)$, showing residue suppression for narrow channels.

scale-dependent residue $\mathcal{D}(q) \propto q^{-\alpha}$ with $\alpha = 1/3$. The suppressed residue is an intrinsic part of the hydrodynamic structure and reflects the spreading of the slowest quasinormal mode over many odd angular harmonics. It would also impact the decay in time of real-space current-current correlations, which take the form $C(x, t) = t^{-\frac{1-\alpha}{z}} f[x/t^{1/z}]$ with $(1 - \alpha)/z = 0.5$ for any value of p . Finally, we note that the dynamical exponent $z = 4/3$ has also appeared in a phenomenological scaling theory of the strange-metal phase [62].

Acknowledgments.— This work was supported by the U.S. Department of Energy, Office of Science, Office of Basic Energy Sciences under Early Career Research Program Award No. DE-SC0025568. DT gratefully acknowledges support from the Eddleman Quantum Institute graduate fellowship. Simulation codes for generating the collision-operator spectrum are available on Github as Ludwig.jl v0.2.1 [63]. We gratefully acknowledge Javier Sanchez-Yamagishi for insightful discussions and Christopher Yang for valuable comments on the manuscript.

* tscaffid@uci.edu

- [1] R. N. Gurzhi, *Soviet Physics Uspekhi* **11**, 255 (1968).
- [2] R. N. Gurzhi, A. N. Kalinenko, and A. I. Kopeliovich, *Physical Review Letters* **74**, 3872 (1995).
- [3] A. Tomadin, G. Vignale, and M. Polini, *Physical Review Letters* **113**, 235901 (2014).
- [4] I. Torre, A. Tomadin, A. K. Geim, and M. Polini, *Physical Review B* **92**, 165433 (2015).
- [5] D. Svintsov, *Physical Review B* **97**, 121405 (2018).

- [6] L. Levitov and G. Falkovich, *Nature Physics* **12**, 672 (2016/07/01, 2016).
- [7] T. Scaffidi, N. Nandi, B. Schmidt, A. P. Mackenzie, and J. E. Moore, *Physical Review Letters* **118**, 226601 (2017).
- [8] A. Lucas, *Physical Review B* **95**, 115425 (2017).
- [9] A. Lucas and K. C. Fong, *Journal of Physics: Condensed Matter* **30**, 053001 (2018).
- [10] A. Lucas and S. A. Hartnoll, *Physical Review B* **97**, 045105 (2018).
- [11] R. Moessner, P. Surówka, and P. Witkowski, *Phys. Rev. B* **97**, 161112 (2018).
- [12] T. Holder, R. Queiroz, T. Scaffidi, N. Silberstein, A. Rozen, J. A. Sulpizio, L. Ella, S. Ilani, and A. Stern, *Physical Review B* **100**, 245305 (2019).
- [13] E. I. Kiselev and J. Schmalian, *Physical Review B* **99**, 035430 (2019).
- [14] E. I. Kiselev and J. Schmalian, *Physical Review Letters* **123**, 195302 (2019).
- [15] A. Levchenko and J. Schmalian, *Annals of Physics* **419**, 168218 (2020).
- [16] X. Huang and A. Lucas, *Physical Review B* **103**, 155128 (2021).
- [17] P. Ledwith, H. Guo, A. Shtyov, and L. Levitov, *Physical Review Letters* **123**, 116601 (2019).
- [18] P. J. Ledwith, H. Guo, and L. Levitov, *Annals of Physics* **411**, 167913 (2019).
- [19] C. Q. Cook and A. Lucas, *Phys. Rev. B* **99**, 235148 (2019).
- [20] A. Stern, T. Scaffidi, O. Reuven, C. Kumar, J. Birkbeck, and S. Ilani, *Physical Review Letters* **129**, 157701 (2022).
- [21] J. Hofmann and S. Das Sarma, *Physical Review B* **106**, 205412 (2022).
- [22] J. Hofmann and U. Gran, *Physical Review B* **108**, L121401 (2023).
- [23] Q. Hong, M. Davydova, P. J. Ledwith, and L. Levitov, arXiv e-prints, arXiv:2012.03840 (2020), arXiv:2012.03840 [cond-mat.mes-hall].
- [24] C. Kumar, J. Birkbeck, J. A. Sulpizio, D. Perello, T. Taniguchi, K. Watanabe, O. Reuven, T. Scaffidi, A. Stern, A. K. Geim, and S. Ilani, *Nature* **609**, 276 (2022).
- [25] J. Estrada-Álvarez, F. Domínguez-Adame, and E. Díaz, *Scientific Reports* **15**, 38326 (2025).
- [26] I. Moiseenko, E. Mönch, K. Kapralov, D. Bandurin, S. Ganichev, and D. Svintsov, *Phys. Rev. Lett.* **134**, 226902 (2025).
- [27] H. Rostami, N. Ben-Shachar, S. Moroz, and J. Hofmann, *Phys. Rev. B* **111**, 155434 (2025).
- [28] J. Estrada-Álvarez, E. Díaz, and F. Domínguez-Adame, *Phys. Rev. Lett.* **135**, 206301 (2025).
- [29] S. Kryhin, Q. Hong, and L. Levitov, *Physical Review B* **111**, L081403 (2025).
- [30] D. Thuillier, S. Ghosh, B. J. Ramshaw, and T. Scaffidi, *Phys. Rev. Lett.*, (2025).
- [31] M. J. M. de Jong and L. W. Molenkamp, *Physical Review B* **51**, 13389 (1995).
- [32] R. Krishna Kumar, D. A. Bandurin, F. M. D. Pellegrino, Y. Cao, A. Principi, H. Guo, G. H. Auton, M. Ben Shalom, L. A. Ponomarenko, G. Falkovich, K. Watanabe, T. Taniguchi, I. V. Grigorieva, L. S. Levitov, M. Polini, and A. K. Geim, *Nature Physics* **13**, 1182 (2017).
- [33] D. A. Bandurin, I. Torre, R. K. Kumar, M. Ben Shalom, A. Tomadin, A. Principi, G. H. Auton, E. Khestanova, K. S. Novoselov, I. V. Grigorieva, L. A. Ponomarenko, A. K. Geim, and M. Polini, *Science* **351**, 1055 (2016).
- [34] A. I. Berdyugin, S. G. Xu, F. M. D. Pellegrino, R. Krishna Kumar, A. Principi, I. Torre, M. Ben Shalom, T. Taniguchi, K. Watanabe, I. V. Grigorieva, M. Polini, A. K. Geim, and D. A. Bandurin, *Science* **364**, 162 (2019).
- [35] J. Crossno, J. K. Shi, K. Wang, X. Liu, A. Harzheim, A. Lucas, S. Sachdev, P. Kim, T. Taniguchi, K. Watanabe, T. A. Ohki, and K. C. Fong, *Science* **351**, 1058 (2016).
- [36] J. A. Sulpizio, L. Ella, A. Rozen, J. Birkbeck, D. J. Perello, D. Dutta, M. Ben-Shalom, T. Taniguchi, K. Watanabe, T. Holder, R. Queiroz, A. Principi, A. Stern, T. Scaffidi, A. K. Geim, and S. Ilani, *Nature* **576**, 75 (2019/12/01, 2019).
- [37] A. Aharon-Steinberg, T. Völkl, A. Kaplan, A. K. Pariari, I. Roy, T. Holder, Y. Wolf, A. Y. Meltzer, Y. Myasoev, M. E. Huber, B. Yan, G. Falkovich, L. S. Levitov, M. Hücker, and E. Zeldov, *Nature* **607**, 74 (2022/07/01, 2022).
- [38] M. L. Palm, C. Ding, W. S. Huxter, T. Taniguchi, K. Watanabe, and C. L. Degen, *Science* **384**, 465 (2024), <https://www.science.org/doi/pdf/10.1126/science.adj2167>.
- [39] J. Geurs, T. A. Webb, Y. Guo, I. Keren, J. H. Farrell, J. Xu, K. Watanabe, T. Taniguchi, D. N. Basov, J. Hone, A. Lucas, A. Pasupathy, and C. R. Dean, *Supersonic flow and hydraulic jump in an electronic de laval nozzle* (2025), arXiv:2509.16321 [cond-mat.mes-hall].
- [40] P. J. W. Moll, P. Kushwaha, N. Nandi, B. Schmidt, and A. P. Mackenzie, *Science* **351**, 1061 (2016).
- [41] N. Nandi, T. Scaffidi, P. Kushwaha, S. Khim, M. E. Barber, V. Sunko, F. Mazzola, P. D. C. King, H. Rosner, P. J. W. Moll, M. König, J. E. Moore, S. Hartnoll, and A. P. Mackenzie, *npj Quantum Materials* **3**, 1 (2018), publisher: Nature Publishing Group.
- [42] M. D. Bachmann, A. L. Sharpe, G. Baker, A. W. Barnard, C. Putzke, T. Scaffidi, N. Nandi, P. H. McGuinness, E. Zhakina, M. Moravec, S. Khim, M. König, D. Goldhaber-Gordon, D. A. Bonn, A. P. Mackenzie, and P. J. W. Moll, *Nature Physics* **18**, 819 (2022).
- [43] Y. Zeng, H. Guo, O. M. Ghosh, K. Watanabe, T. Taniguchi, L. S. Levitov, and C. R. Dean, *Quantitative measurement of viscosity in two-dimensional electron fluids* (2024), arXiv:2407.05026 [cond-mat.mes-hall].
- [44] V. B. Bulchandani, C. Karrasch, and J. E. Moore, *Proceedings of the National Academy of Sciences* **117**, 12713 (2020), <https://www.pnas.org/doi/pdf/10.1073/pnas.1916213117>.
- [45] M. Ljubotina, M. vZnidarivc, and T. Prosen, *Physical Review Letters* **122**, 210602 (2019).
- [46] F. Weiner, P. Schmitteckert, S. Bera, and F. Evers, *Physical Review B* **101**, 045115 (2020).
- [47] M. Dupont and J. E. Moore, *Phys. Rev. B* **101**, 121106 (2020).
- [48] K. A. Takeuchi, K. Takasan, O. Busani, P. L. Ferrari, R. Vasseur, and J. De Nardis, *Physical Review Letters* **134**, 097104 (2025).
- [49] B. Doyon, S. Gopalakrishnan, F. Møller, J. Schmiedmayer, and R. Vasseur, *Phys. Rev. X* **15**, 010501 (2025).
- [50] K. G. Nazaryan and L. Levitov, *Physical Review B* **110**, 045147 (2024).
- [51] G. A. Starkov and B. Trauzettel, *Phys. Rev. B* **113**,

L041406 (2026).

- [52] J. Maki and J. Hofmann, [arXiv e-prints](#), [arXiv:2603.06518](#) (2026), [arXiv:2603.06518 \[cond-mat.str-el\]](#).
- [53] We will take $v_F = 1$ throughout except when we give numerical estimates.
- [54] See supplemental material at [url] for additional details on computing the collision operator spectrum, the low temperature model spectrum and the asymptotics of the even spectrum, defining the basis for the krylov chain, computing the current profile in a channel, and the spectrum of l_q which includes refs. [17, 30, 50, 55, 56].
- [55] E. Nilsson, U. Gran, and J. Hofmann, [Physical Review X](#) **15**, 041007 (2025).
- [56] S. M. Blinder, [Eigenvalues for a pure quartic oscillator](#) (2019), [arXiv:1903.07471 \[quant-ph\]](#).
- [57] D. E. Parker, X. Cao, A. Avdoshkin, T. Scaffidi, and

E. Altman, [Phys. Rev. X](#) **9**, 041017 (2019).

- [58] Upon taking the continuum limit, the first Krylov site — corresponding to the current — maps to $m = 0$, and the original semi-infinite chain may be unfolded to the full real line provided one restricts to wavefunctions even under $m \rightarrow -m$.
- [59] As discussed in the SM, for a quartic oscillator, $\epsilon_1/\epsilon_0 \approx 7$.
- [60] The prefactor is ne^2/m with n the density and m the mass.
- [61] G. Baker, T. W. Branch, J. S. Bobowski, J. Day, D. Valentinis, M. Oudah, P. McGuinness, S. Khim, P. Surówka, Y. Maeno, T. Scaffidi, R. Moessner, J. Schmalian, A. P. Mackenzie, and D. A. Bonn, [Phys. Rev. X](#) **14**, 011018 (2024).
- [62] S. A. Hartnoll and A. Karch, [Phys. Rev. B](#) **91**, 155126 (2015).
- [63] Davis Thuillier, [Ludwig.jl](#) (2024).

End Matter

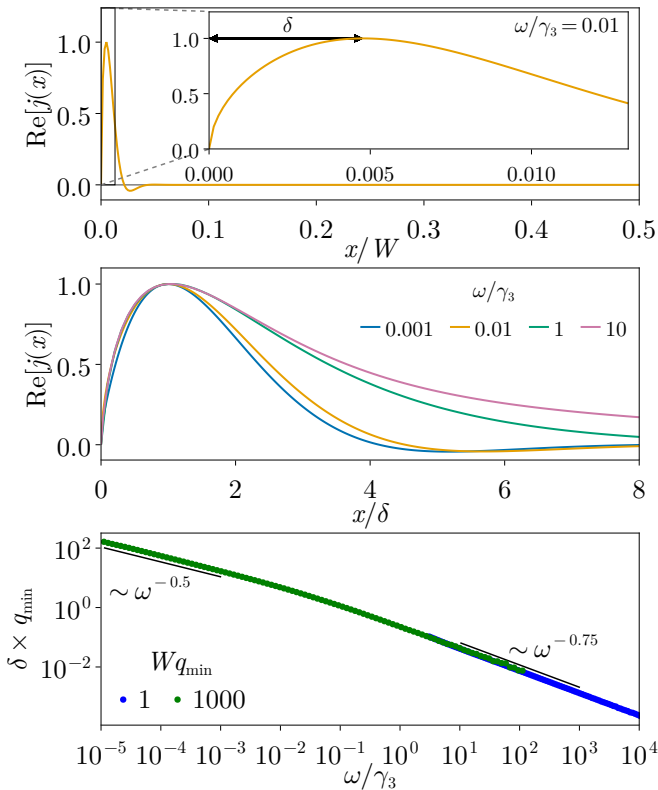


FIG. 5. Top: current profile for the model spectrum at $T/T_F = 10^{-5}$ in a channel of width $W = 1000 q_{\min}^{-1}$ with no-slip boundary conditions. The maximum of $\text{Re}[j(x)]$ defines the boundary-layer width δ . Middle: collapse of the current profiles under rescaling by δ . The crossover near $\omega \sim \gamma_3$ is accompanied by a qualitative change in the decay into the bulk. Bottom: frequency dependence of δ , showing the crossover from $\delta \sim \omega^{-1/2}$ for $\omega \ll \gamma_3$ to $\delta \sim \omega^{-3/4}$ for $\omega \gg \gamma_3$.

Current profiles and boundary layers.— The current profile in a channel can be obtained from $\sigma(q, \omega)$ following Ref. [17]; see SM for details. We compute $j(x)$ by solving the Boltzmann equation in a channel of width W

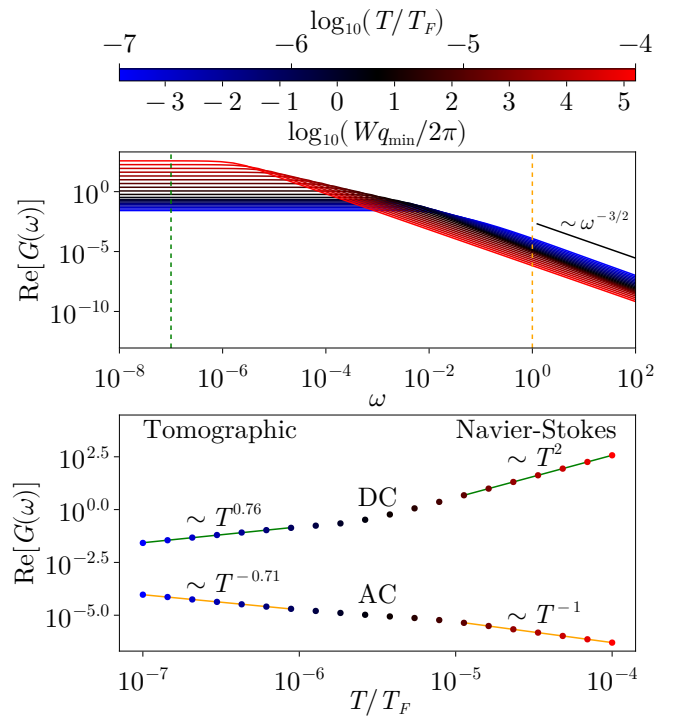


FIG. 6. Top: channel conductance as a function of $\omega/q_{\min}(T_0)$ for fixed width $W = 0.001 q_{\min}^{-1}(T_0)$, where $T_0/T_F = 10^{-7}$. Blue and red respectively denote temperatures with $q_{\min}(T) < 2\pi/W$ and $q_{\min}(T) > 2\pi/W$. Bottom: temperature dependence of the conductance at low (DC) and high (AC) frequencies (the two vertical lines in top panel show the two frequency values). The Navier–Stokes regime, at higher T/T_F , shows the expected T^2 scaling at low frequency and T^{-1} scaling at high frequency. The tomographic range (smaller T/T_F) shows a different scaling with temperature, with extracted scaling $T^{0.76}$ for DC and $T^{-0.71}$ for AC. These exponents are lower than the ones predicted deep in the tomographic regime (T^{+1} scaling for DC and T^{-1} for AC) due to the slow drift of exponents.

with strong boundary scattering. In the low-frequency tomographic regime, the current profile is well described by $\sim x^{1/3}(W-x)^{1/3}$, as previously reported in Ref. [17]. At higher frequency, when $\omega \gg \eta_* W^{-z}$, a boundary layer of width $\delta \sim (\eta/\omega)^{1/z}$ develops near each wall, beyond which the real part of the current decays strongly and the bulk response becomes predominantly reactive.

This behavior is illustrated in Fig. 5. The top and middle panels show representative profiles of $\text{Re } j(x)$ localized within a width δ near the boundaries. The bottom panel shows the corresponding scaling of δ with frequency, revealing a clear crossover from the Navier–Stokes form $\delta \propto \sqrt{\eta/\omega}$ at $\omega \ll \gamma_3$ to the tomographic form $\delta \propto (\eta_*/\omega)^{3/4}$ at $\omega \gg \gamma_3$. At fixed ω , these two regimes also differ in their temperature dependence: $\delta_{\text{NS}} \propto T^{-1}$ whereas $\delta_{\text{tomog}} \propto T^{4-3z}$. Since $z \rightarrow 4/3$ asymptotically, the tomographic boundary-layer width becomes nearly temperature independent deep in the asymptotic regime. The middle panel of Fig. 5 further suggests that the decay into the bulk is slower than exponential in the tomographic regime, presumably because the nonlocal conductivity is nonanalytic in q .

Channel-conductance scaling.— We now discuss the dependence of the channel conductance on temperature, width, and frequency; see Fig. 6. In that figure we fix the width and vary T/T_F , allowing us to scan from the Navier–Stokes regime at higher temperatures to the tomographic regime at lower temperatures. In the low-frequency limit, the relevant distinction is whether $Wq_{\text{min}} \gg 1$ (Navier–Stokes) or $Wq_{\text{min}} \ll 1$ (tomographic). In the first case, one finds

$$\frac{G}{W} \sim \frac{W^2}{\eta} \propto T^2 \quad (\text{Navier–Stokes}), \quad (\text{A1})$$

whereas in the tomographic regime

$$\frac{G}{W} \sim \frac{q_{\text{min}}^\alpha W^{z+\alpha}}{\eta_*} \propto T^{3(z+\alpha)-4}. \quad (\text{A2})$$

Deep in the asymptotic tomographic regime, $z + \alpha \rightarrow 5/3$, recovering the linear-in- T conductance predicted in Ref. [29]. In practice, however, the logarithmic drift of the exponents remains substantial even at ambitious values of T/T_F and Wq_{min} , as seen in the lower panel of Fig. 6, where the numerical DC conductance scales approximately as $T^{0.76}$. This may be important when comparing quantitatively with experiments extracting viscosities, such as Ref. [43].

At higher frequency, the relevant comparison is between the skin depth δ and the tomographic length q_{min}^{-1} . Either way, the high-frequency conductance behaves parametrically as

$$\begin{aligned} \text{Re } G &\sim \frac{\delta}{\omega} (q_{\text{min}} \delta)^{-\alpha}, \\ \text{Im } G &\sim \frac{W}{\omega}. \end{aligned} \quad (\text{A3})$$

These expressions reduce correctly to both the Navier–Stokes regime, where $\alpha = 0$ and $\delta = \sqrt{\eta/\omega}$, and the tomographic regime, where $\alpha = 1/3$ and $\delta = (\eta_*/\omega)^{3/4}$. As expected, $\text{Re } G$ becomes independent of W at high frequency because only the boundary layers contribute appreciably to the in-phase current.

In the Navier–Stokes regime this gives

$$\text{Re } G \sim \frac{1}{\omega^{3/2} \sqrt{\gamma_2}} \propto T^{-1}, \quad (\text{A4})$$

whereas in the tomographic regime we find

$$\text{Re } G(\omega) \sim \frac{1}{\omega^{\frac{p_{\text{eff}}}{2p}+1} \sqrt{\gamma_2} \gamma_3^{-\frac{p_{\text{eff}}}{2p}+\frac{1}{2}}} \propto T^{-3+2p_{\text{eff}}/p}, \quad (\text{A5})$$

with $p_{\text{eff}}/p = 2(1 - \alpha(q))/z(q)$ encoding the drift of the apparent exponents. Asymptotically, $p_{\text{eff}} \rightarrow p$ and the high-frequency temperature dependence approaches the same T^{-1} scaling as in the Navier–Stokes regime, even though the spatial structure of the current remains very different. The frequency scaling is confirmed in the top panel of Fig. 6; the lower panel shows that the temperature scaling in the tomographic regime still exhibits substantial drift, with an observed behavior close to $T^{-0.71}$ for the parameters used there.

Supplemental material to “AC Fingerprints of 2D Electron Hydrodynamics: Superdiffusion and Drude Weight Suppression”

Appendix A: Computing the spectrum of the collision operator L

Applying the method we introduced in [30], we performed a direct calculation of the linearized electron-electron collision operator for a single parabolic band with short-range repulsion. The collision integral kernel $\mathcal{L}(\mathbf{k}_1, \mathbf{k}_2)$ can be expressed in terms of energy-angle coordinates. Due to rotational symmetry and mirror symmetry about $(\mathbf{k} + \mathbf{k}')/2$, the kernel is an even function of the angular difference, $\theta = \theta_1 - \theta_2$ between the momenta. For each harmonic, we can then integrate out this angular dependence to define $\mathcal{L}_m(\varepsilon, \varepsilon') = \int d\theta \cos(m\theta) \mathcal{L}(\varepsilon, \varepsilon', \theta)$. In practice, momenta are sampled on an energy-angle grid with n_ε points sampled along the energy direction and n_θ points sampled in angle. \mathcal{L}_m is thus represented by an $n_\varepsilon \times n_\varepsilon$ matrix.

We define the rate γ_m to be the minimal magnitude eigenvalue of the \mathcal{L}_m matrix. It is possible to replace the scalar rates in the continued fraction method of Nazaryan and Levitov [50] with the \mathcal{L}_m matrices and evaluate the nonlocal conductivity by taking the inner product $\langle v(\varepsilon) | \hat{\Gamma}_q | v(\varepsilon) \rangle$ where $\hat{\Gamma}_q$ denotes the corresponding *operator continued fraction*. However, larger eigenvalues in each block correspond to short-lived eigenfunctions having weak overlap with the rigid chemical potential shift we consider, and thus do not contribute substantially to the conductivity.

Modeling the spectrum at low- T .— As temperature is lowered, the error of all rates scales as $1/n_\varepsilon$ for fixed angular resolution (standard Riemannian integration error). However, the error of the lowest odd rates ($m = 3, 5, 7, \dots$) increases relative to the rest of the spectrum as temperature is lowered, demanding n_ε be increased to achieve the same level of convergence. The computation time for L is $\mathcal{O}((n_\theta n_\varepsilon)^3)$, so the convergence of the odd rates ultimately limits the minimal temperature for which L can be computed in fixed time. In order to compute dynamics at lower temperatures than achievable through direct computation of L , we turn to modeling the spectrum at small m .

The even rates in Figure 1 shown plotted against the logarithm of m are linear over a region which scales as $\sim 1/\sqrt{T/T_F}$. As temperature is lowered, we find improved agreement to the low-temperature analytical model spectrum from [55], whose asymptotic form (discussed in Appendix C) grows logarithmically with m .

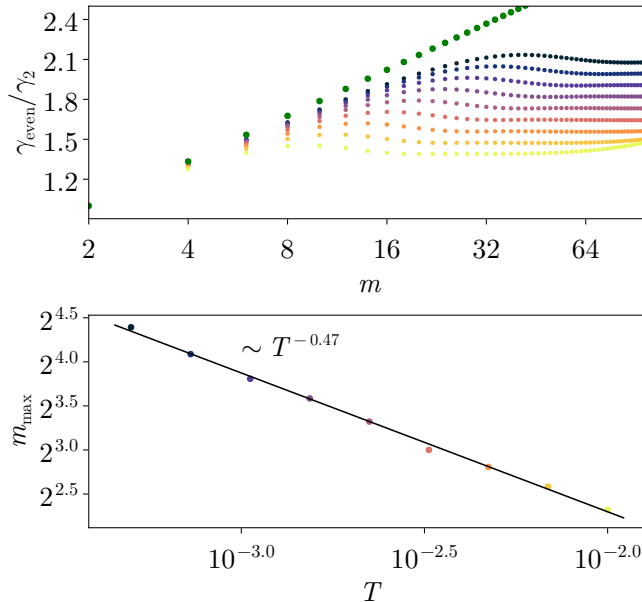


FIG. 1. Semi-log plot of the even spectra with the low temperature analytical model shown in green. As temperature is lowered, the lowest even modes collapse onto the model spectrum over a region which grows as $\sim 1/\sqrt{T/T_F}$.

Appendix B: Low-temperature model spectrum

From Nilsson *et al.* [55], the even rates for small m are given by

$$\gamma_{m,\text{even}} = \frac{8\pi T_F}{3\hbar} \left(\frac{T}{T_F}\right)^2 \frac{|V|^2}{\lambda_T^2} F[m] \equiv \gamma_2 F[m] \quad (\text{S1})$$

for a constant interaction matrix element V and λ_T the thermal de Broglie wavelength, with $F[m] = \sum_{j=1}^{m/2} \frac{1}{2j-1}$ a slowly increasing function of m with $F[2] = 1$ and $F[m \rightarrow \infty] \sim \frac{1}{2} \log(m)$ (see Appendix C). In the small m region, Nilsson *et al.* [55] further found analytically that, for $m \geq 3$,

$$\gamma_{m,\text{odd}} = \frac{4\pi^3 T_F}{15\hbar} \frac{|V|^2}{\lambda_T^2} m^4 \left(\frac{T}{T_F}\right)^4 \equiv \gamma_3 \left(\frac{m}{3}\right)^4. \quad (\text{S2})$$

Appendix C: Asymptotic Limit of $F[m]$

The series $F[m]$ which defines the rise of the even rates can be expressed in terms of harmonic numbers:

$$\begin{aligned} \sum_{j=1}^{m/2} \frac{1}{2j-1} &= 1 + \frac{1}{3} + \cdots + \frac{1}{m+1} \\ &= 1 + \frac{1}{2} + \frac{1}{3} \cdots + \frac{1}{m+1} \\ &\quad - \frac{1}{2} \left(1 + \frac{1}{2} + \cdots + \frac{1}{m/2}\right) \\ &= H_m - \frac{1}{2} H_{m/2} \end{aligned} \quad (\text{S1})$$

where $H_m = \sum_{j=1}^m \frac{1}{j}$ denotes the m^{th} harmonic number. By definition, the Euler-Mascheroni constant is given by $\gamma \equiv \lim_{m \rightarrow \infty} (H_m - \ln m)$. Thus, in the asymptotic limit,

$$\begin{aligned} \sum_{j=1}^{m/2} \frac{1}{2j-1} &\approx \gamma - \ln m - \frac{1}{2}(\gamma - \ln \frac{m}{2}) \\ &= \frac{1}{2} \left(\ln \frac{m}{2} + \gamma \right) \end{aligned} \quad (\text{S2})$$

Appendix D: AC current profiles in a channel

Current profiles.— We consider transport in an infinite 2D channel, $0 < x < W$, where the current is driven by an electric field $\mathbf{E} = E e^{i\omega t} \hat{y}$. From [17], extended to finite frequency, the current profile for no-slip boundary conditions reads

$$j(x) = E \frac{\sum_{n \neq 0} \sigma(q_n, \omega) - \sum_{n \neq 0} \sigma(q_n, \omega) e^{iq_n x}}{1 + \sum_{n \neq 0} \sigma(q_n, \omega) / \sigma(0, \omega)} \quad (\text{S1})$$

with $q_n = 2\pi n/W$, and $\sigma(0, \omega) = 1/(i\omega + \gamma_{\text{mr}})$. We used this formula to calculate numerically the current profiles shown in Fig 5 of the main text.

Channel conductance scaling.— The channel conductance, $G(\omega)$, can be obtained by integrating over x giving:

$$G(W, \omega) = \frac{W}{i\omega + \gamma_{\text{mr}} + (\sum_{n \neq 0} \sigma(q_n, \omega))^{-1}} \quad (\text{S2})$$

where γ_{mr} denotes the scattering rate corresponding to momentum-relaxing collisions which we will take to be zero in the rest of this appendix.

	Viscous	Tomographic
$\omega = 0$	2	$3(z + \alpha) - 4$
$\omega \rightarrow \infty$	-1	$-3 + 4(1 - \alpha)/z$

TABLE I. Temperature scaling exponents of $\text{Re}[G(\omega)]$.

One can now ask what the asymptotic scaling of $G(\omega)$ is for the single pole approximation of the conductivity, $\sigma(q, \omega) = (q/q_{\min})^{-\alpha}/(i\omega + \eta_{\star}q^z)$. Let $S = \sum_{n>0} \sigma(q_n, \omega)$ and define the dimensionless frequency $\Omega = \omega(W/2\pi)^z/\eta_{\star}$. We find

$$S = \left(\frac{W}{2\pi}\right)^{\alpha+z} \frac{q_{\min}^{\alpha}}{\eta_{\star}} \sum_{n>0} \frac{n^{-\alpha}}{i\Omega + n^z} \quad (\text{S3})$$

In the DC limit $\Omega \rightarrow 0$, the sum is just a numerical constant, and thus

$$\begin{aligned} \text{Re}[G(W, \omega = 0)] &= W \text{Re}[S] \\ &\sim W^{1+\alpha+z} q_{\min}^{\alpha} \eta_{\star}^{-1} \end{aligned} \quad (\text{S4})$$

In the Navier-Stokes regime ($\alpha = 0, z = 2, \eta_{\star} = \eta \sim \gamma_2^{-1}$), this specifies to

$$\text{Re}[G(W, \omega = 0)] \sim W^3 \eta^{-1} \propto W^3 T^2 \quad (\text{S5})$$

For the tomographic regime, the T scaling then reads

$$\text{Re}[G(W, \omega = 0)] \propto W^{1+\alpha+z} T^{3(z+\alpha)-4} \quad (\text{S6})$$

where we used the fact that $\eta_{\star} \sim T^{4-3z}$.

In the high frequency limit, the summand becomes negligible above $n_{\max} \sim |\Omega|^{1/z}$. Thus the magnitude of S scales as:

$$\begin{aligned} |S| &\sim \left(\frac{W}{2\pi}\right)^{\alpha+z} \frac{q_{\min}^{\alpha}}{\eta_{\star}} n_{\max} \left[\frac{n_{\max}^{-\alpha}}{n_{\max}^z} \right] \\ &\sim \left(\frac{W}{2\pi}\right)^{\alpha+z} \frac{q_{\min}^{\alpha}}{\eta_{\star}} |\Omega|^{(1-\alpha-z)/z} \\ &\sim \frac{q_{\min}^{\alpha}}{\eta_{\star}^{(1-\alpha)/z}} \left(\frac{W}{2\pi}\right) \omega^{\frac{1-\alpha}{z}-1} \end{aligned} \quad (\text{S7})$$

Note that S has both a real and imaginary parts that of the same order.

In the high frequency limit, the scaling of the real part of the conductance is then given by

$$\begin{aligned} \text{Re}[G(\omega)] &\approx W \frac{\text{Re}[S^{-1}]}{\omega^2} \quad \text{for } \Omega \gg 1 \\ &\sim q_{\min}^{-\alpha} \eta_{\star}^{\frac{1-\alpha}{z}} \omega^{-\frac{1-\alpha}{z}-1} \end{aligned} \quad (\text{S8})$$

In the Navier-Stokes regime, this simplifies to

$$\text{Re}[G(\omega)] \sim \eta^{\frac{1}{2}} \omega^{-3/2} \propto \frac{1}{T \omega^{3/2}} \quad (\text{S9})$$

In the tomographic regime, one finds instead

$$\text{Re}[G(\omega)] \sim q_{\min}^{-1} \gamma_3^{\frac{1-\alpha}{z}} \omega^{-\frac{1-\alpha}{z}-1} \propto T^{-3+4\frac{1-\alpha}{z}} \omega^{-\frac{1-\alpha}{z}-1} \quad (\text{S10})$$

The scaling with temperature is summarized in [Table I](#).

Appendix E: Krylov gauge transformation

Starting from the BTE in the basis of real cylindrical harmonics, $\varphi_{m,\text{odd}} = \cos(m\theta)$, $\varphi_{m,\text{even}} = \sin(m\theta)$.

$$\partial_t \varphi_m = (-1)^m \frac{iqv_F}{2} (\varphi_{m+1} - \varphi_{m-1}) - \gamma_m \varphi_m. \quad (\text{S1})$$

Define a parity-dependent phase (“gauge”) transformation

$$\tilde{\varphi}_m \equiv i^{a_m} \varphi_m, \quad a_m \equiv \frac{1 + (-1)^m}{2} = \begin{cases} 1, & m \text{ even,} \\ 0, & m \text{ odd.} \end{cases} \quad (\text{S2})$$

Equivalently, $\varphi_m = i^{-a_m} \tilde{\varphi}_m$.

Substituting $\varphi_{m\pm 1} = i^{-a_{m\pm 1}} \tilde{\varphi}_{m\pm 1}$ into (S1) and multiplying both sides by i^{a_m} yields

$$\partial_t \tilde{\varphi}_m = (-1)^m i^{a_m - a_{m+1}} \frac{iqv_F}{2} (\tilde{\varphi}_{m+1} - \tilde{\varphi}_{m-1}) - \gamma_m \tilde{\varphi}_m. \quad (\text{S3})$$

Now note

$$a_m - a_{m+1} = \frac{1}{2} \left[(1 + (-1)^m) - (1 + (-1)^{m+1}) \right] = (-1)^m. \quad (\text{S4})$$

Therefore,

$$(-1)^m i^{a_m - a_{m+1}} = (-1)^m i^{(-1)^m} = \begin{cases} i, & m \text{ even,} \\ i, & m \text{ odd,} \end{cases} = i, \quad (\text{S5})$$

so the hopping prefactor becomes

$$\left[(-1)^m i^{a_m - a_{m+1}} \right] \frac{iqv_F}{2} = i \cdot \frac{iqv_F}{2} = -\frac{qv_F}{2}. \quad (\text{S6})$$

Plugging this into (S3), we obtain

$$\partial_t \tilde{\varphi}_m = -\frac{qv_F}{2} (\tilde{\varphi}_{m+1} - \tilde{\varphi}_{m-1}) - \gamma_m \tilde{\varphi}_m. \quad (\text{S7})$$

which is the form used in the main text.

Appendix F: Spectrum of the Liouvillian L_q and the quasi-normal mode

The decay rate of the Krylov wavefunction at late times is identified with the minimal eigenvalue of the Liouvillian, $L_q \equiv L + i\mathbf{q} \cdot \mathbf{v}$. In Figure 2, this eigenvalue is identified in red.

The Krylov picture corresponds to the problem of the quartic oscillator, $-\psi''(x) + \frac{1}{2}|x|^4\psi(x) = E\psi(x)$ under reflecting boundary conditions at $x = 0$. The two lowest eigenvalues of L_q therefore correspond to the two lowest *even parity* eigenvalues of the quartic oscillator on the whole real line. These energies have been solved numerically [56], and it can be shown that $E_0 = 0.420805$, $E_2 = 2.95886$, such that $E_2/E_0 \approx 7.03$.

At $q = 10q_{\text{min}}$, the ratio of the two lowest eigenvalues is 7.04, and this ratio holds approximately across the entire tomographic plateau. This separation ensures that at late times, the dynamics of the Krylov wavefunction is indeed dominated by a single quasinormal mode for all q in the tomographic regime.

For all q , $\text{Im}[\gamma(q)]$ is bounded by $\pm qv_F$. In the ballistic limit, $qv_F \gg \gamma_m$, the real part of $\gamma(q)$ can be neglected, and each mode propagates as a plane wave with frequency qv_F .

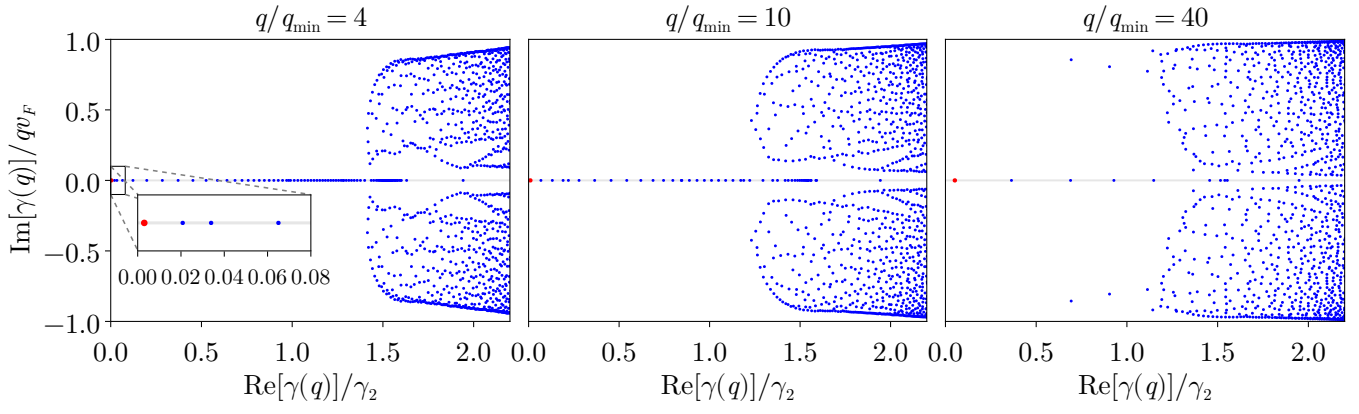


FIG. 2. Spectrum of L_q for $T/T_F = 0.005$ at three values of q in the tomographic regime. The red dot identifies the eigenvalue with minimal real part; i.e., the late-time decay rate of the Krylov wavefunction.